



CuO Nanoparticle-Protein Bioconjugate: Characterization of CuO Nanoparticles for the Study of the Interaction and Dynamic of Energy Transfer with Bovine Serum Albumin

Amit Kumar Bhunia¹ · Satyajit Saha²

Published online: 5 November 2019
© Springer Science+Business Media, LLC, part of Springer Nature 2019

Abstract

Here, we aim to disclose the role of two different ranges concentration of copper oxide nanoparticles (CuO NPs) for the adsorption of BSA to CuO NP surfaces and the kinetics of the energy transfer between CuO NPs and BSA molecule by using different spectroscopy, time-resolved fluorescence measurements, and DLS study. The grown ~ 20.31 nm CuO NPs showed 3.60-eV band gap and 1.026-eV Urbach energy. The XRD pattern showed that the unit cell of the synthesized CuO nano-crystal is monoclinic phase. The photoluminescence spectrum of pure CuO NPs showed a high quantum yield of the blue emission. A small red shift of the absorption peak of BSA is determined because of binding with CuO NPs. The calculated value of an apparent association constant (K_{app}) in the CuO NPs–BSA bioconjugate was found to be $6.51 \times 10^3 \text{ M}^{-1}$ and $2.16 \times 10^3 \text{ M}^{-1}$ for the small concentration range and large concentration range, respectively. The total change in energy transfer efficiency (ΔE_{eff}) at room temperature is 22% and 5.6% for the use large and small concentration, respectively; at body temperature, this change is 13.6% and 6.6%, respectively. The BSA quenching is a mixed type in lower temperature in the low-concentration range and fully dynamic in the high-concentration range. The nature of interaction is exothermic, electrostatic, and hydrophobic. The fluorescence lifetimes of pure BSA decreased from 4.94 to 1.04 ns upon adsorption onto CuO NPs, corresponding to E_{eff} of 79.35%. The use of large concentration leads to aggregation rather than individual corona formation under the small concentration of CuO NPs.

Keywords CuO nanoparticles · Absorption · Fluorescence quenching · Energy transfer · Protein-nanoparticle interaction

1 Introduction

Recently, the good interests in producing and demand of metal oxide nanoparticles in commercial and industrial merchandise have led to target on the potential influence of these particles on biomedicine. In this field, copper-based nanoparticles in an area unit are an issue of nice interest in recent years because of their distinctive physical and chemical properties [1]. Copper oxide (CuO) could be a semiconductor compound with a

monoclinic structure. It has fascinated large captivate as a result of having the simplest structure of the family of copper compounds and reveals a variety of potentially helpful physical application like catalysts and biomedical application. Copper oxide (CuO) has attracted attention largely owing their antimicrobial and biocide properties and its other biomedical applications [2, 4]. Few metal oxide nanoparticles, like zinc oxide (ZnO) and copper oxide (CuO), have antimicrobial and antifungal properties that construct them, ideal for a variety of coating applications. Nanostructure CuO is employed in textile fibers, coatings, and thermoplastics to inhibit microbial and fungal growth, additives for ceramics process and colorants, and pigments for different materials [2–4]. Copper oxide-based nanofibrillar cellulose may be a promising biomaterial [5]. The unique properties of CuO nanocrystals are significantly interested in the biomedical field increases rapidly. Copper oxide nanoparticles are also used as contrast agents for MRI and ultrasound dual-modality imaging. However, before going into realizing the medical specialty applications, it is greatly essential to grasp the means, nature, and condition of the interaction of clean CuO NPs with

Electronic supplementary material The online version of this article (<https://doi.org/10.1007/s12668-019-00687-z>) contains supplementary material, which is available to authorized users.

✉ Amit Kumar Bhunia
amitphysics87@gmail.com

¹ Department of Physics, Government General Degree College at Gopiballavpur-II, Beliaberah, Jhargram, West Bengal 721517, India

² Department of Physics, Vidyasagar University, Paschim Medinipur, West Bengal 721102, India

protein. However, before going into realizing the biomedical applications, it is very much essential to understand the way, nature, and condition of the interaction of bare CuO NPs with plasma protein. The risks of exposing to nanocrystals for human are sometimes toxic and may be accidental. The most important disadvantage of their use in the medical domain is due to their potentially toxic effects [4, 6–8]. CuO NPs can also be toxic to mammalian cells as well as for vertebrates and invertebrates [9, 10]. They also interact with various biomolecules. The CuO NPs directly or indirectly come in contact with the interfaces of different biomolecules including the protein of our body under different biomedical applications. When nanoparticles come in contact with protein molecules, they form a nanoparticle-protein corona and interact with protein molecules. The effect of this CuO NPs on the different biomolecules is different. They interact with different biomolecules including protein molecules due to a large surface free energy in nano-domain biomedicine under contact with our body. The research for the effect of CuO NPs on protein molecules is very few [11–14]. Nanoparticle-protein interaction depends on various parameters like particle size, shape, the chemical composition of its surface, ζ potential and surface hydrophobicity, pH of the solution, nature of the protein, and temperature [15–20]. Also, the concentrations of nanoparticles and the nature of biological fluid can influence the result of identification experiments [21]. Different ranges of concentration-dependent serum protein adsorption at the nano-bio interfaces is studied solely few researchers [22]. Here, we focused the role of CuO NPs concentration due to interaction with BSA protein by spectroscopic and microscopic techniques, mainly focused on the two different ranges of concentrations. We studied in details about the long-time dynamics of the energy transfer mechanism under different conditions. We used the bovine serum albumin (BSA) as a model protein because it is inexpensive, easily accessible, and structurally more similar to human serum albumin (HSA).

2 Experimental

2.1 Synthesis of CuO Nanoparticles and Bioconjugate Preparation

In the synthesis of CuO NPs at room temperature, we accompanied the chemical precipitation method for the synthesis of CuO nanostructures. In this technique, 2.5 g copper acetate was dissolved in 50 mL deionized water and stirred in the magnetic stirrer for a few minutes, then 1.00 g NaOH in 50 mL water solution was added drop-wise under a vigorous stirring condition. The pH of the solution is maintained ~ 10 . After the complete addition of the NaOH solution within the copper acetate solution, the magnetic stirring was continuing for 2 h. The reaction solution is kept at 35 °C overnight. The

product was filtered and washed by di-water several times. The final product power was annealed by a muffle furnace under 300 °C for 2 h. Then the sample is cooled into room temperature and collected for characterization. The BSA solutions with a preset concentration of BSA ($C_{\text{BSA}} = 0.01$ mg/mL) was ready by exploitation triple distilled water, deionized with a Milli-Q water purification system from Millipore, USA. The pH and the resistivity of freshly ready water were 6.8 and 18.2 M Ω cm, severally. The ready CuO NPs were dispersed in deionized Millipore water by ultrasonication for 60 min. The concentration of the CuO was varied from 12.5 to 1257.16 μM . CuO NPs–BSA mixed solutions were prepared by mixing 0.001 mg/mL BSA with CuO, ranging from 12.5 μM to 1257.17 μM with proper ratio.

2.2 Characterization Methods

See supplementary S1.

3 Results and Discussion

3.1 Absorption Spectrum

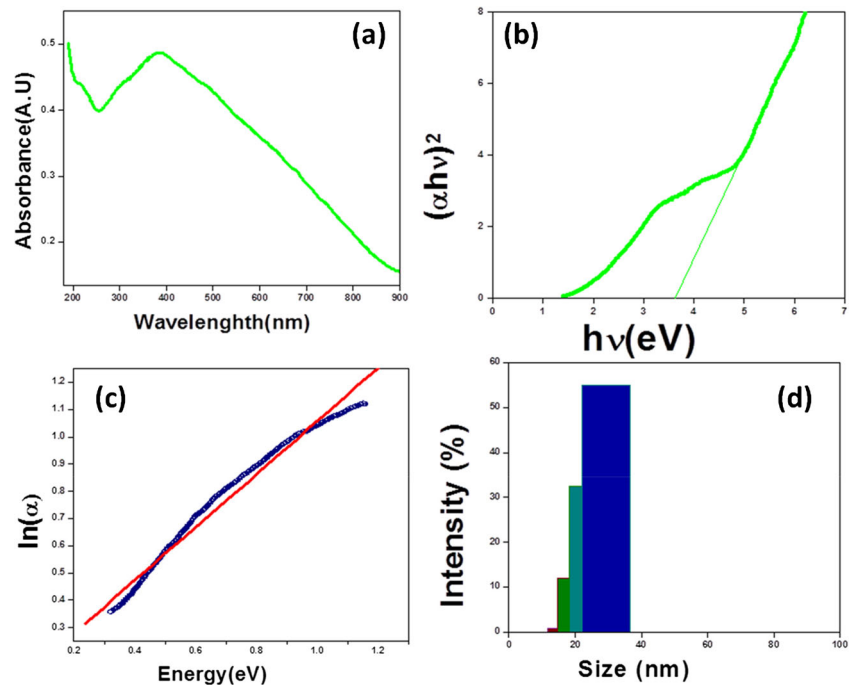
The optical absorption is studied with in wavelength range 200 nm to 900 nm. The observed optical absorption spectrum for the variation of optical absorbance of the grown CuO NPs dispersed in water is shown in Fig. 1a. The maximum absorbance peak was seen at ≈ 385.25 nm. The optical absorption coefficient (α) has been calculated from the Lambert law in the wavelength region 200–900 nm [23]. The optical band gap (E_g) of the as-arranged nanoparticles have been figured utilizing the Tauc equation [24]:

$$(\alpha h\nu)^2 = c(h\nu - E_g)$$

Here, $\alpha = 2.303 A/t$ (A = absorbance). Figure 1b demonstrates the plot of $(\alpha h\nu)^2$ vs. energy ($h\nu$), and it is utilized to decide band gap. The estimated direct band gap is 3.60 eV. This band gap esteem is greater than bulk CuO (3.25 eV) reported by Koffyberg et al. [25]. The greater band gap formation in CuO nanostructure was reported by Klinbumrung et al. [26]. The watched increment in the direct bandgap esteems (a blue move) of CuO with the diminishing in nanoparticle estimate is ascribed to the quantum-confinement. Wavelength reliance of optical absorption property of semiconductor can be communicated by the following condition [27]:

$$\alpha = \alpha_0 \exp \left[\frac{h\nu}{E_u} \right]$$

Fig. 1 **a** Absorption spectroscopy of CuO NPs. **b** Bandgap determination plot. **c** Plot of $\ln(\alpha)$ versus photon energy ($h\nu$) of the CuO nanoparticles. **d** Dynamic light scattering (DLS) spectrum of pure CuO NPs



By plotting $\ln(\alpha)$ with the incident photon energy $h\nu$, the Urbach energy E_U can be resolved. The variation of $\ln(\alpha)$ with the incident photon energy $h\nu$ appeared in Fig. 1c. Urbach energy is acquired from the inverse of the incline (see Fig. 1c). The calculated value of the Urbach energy is 1.026 eV, which is near the announced estimation of 1.01 eV [28]. This minor change from other reported value of Urbach energy may be due to the crystal disorder, temperature, bondings, and change in average photon energies [29].

3.2 Emission Spectrum

Figure 2a and 2b show the photoluminescence spectrum of CuO NPs under two different excitation wavelengths; one is 320 nm and another is 340 nm, respectively. The emission peaks corresponding to excitation (λ_{ext}) at 320 nm are observed at 426.399 nm, 459.51 nm, and 486.51 nm [30, 31]. The first one corresponds to the band edge emission in the violet region. The second is because of the oxygen vacancies arise in the blue region. The third one arises from the multiple oxidation states of copper in the blue region. The quantum yield of the blue emission peak corresponding to oxygen vacancies is larger compared with other regions of the wavelengths. The quantum yield is directly proportional with the area of the Gaussian fitting at the emission maxima (see supplementary S2 (a)). The emission peaks (λ_{em}) corresponding to excitation at 340 nm are observed at 458.75 nm and 487.96 nm [32]. The quantum yield of the blue emission peak at 487.96 nm is larger compared with the peak at 458.75 nm (see supplementary S2 (b)). The corresponding energy levels are tabulated in Tables 1 and 2.

3.3 Dynamic Light Scattering

The hydrodynamic size of the grown CuO NPs is measured by the DLS technique [33]. All sizes reported here were supported intensity average. The variation of intensity (%) with size (nm) is shown in Fig. 1d. The light scattering of the CuO nanoparticles (Fig. 1d) dispersed in water showed that the particles are mono dispersed with an average hydrodynamic size of ~ 24 nm.

3.4 XRD

The XRD pattern shown in Fig. 2c shows that the unit cell of the synthesized CuO nano-crystal is monoclinic with the presence of the peaks (110), ($\bar{1}$ 11), (111), ($\bar{2}$ 02), (020), (202), ($\bar{1}$ 13), (022), (220), ($\bar{3}$ 12), and (203) [34, 35]. The nanoparticle size is calculated from the Scherrer formula [36]:

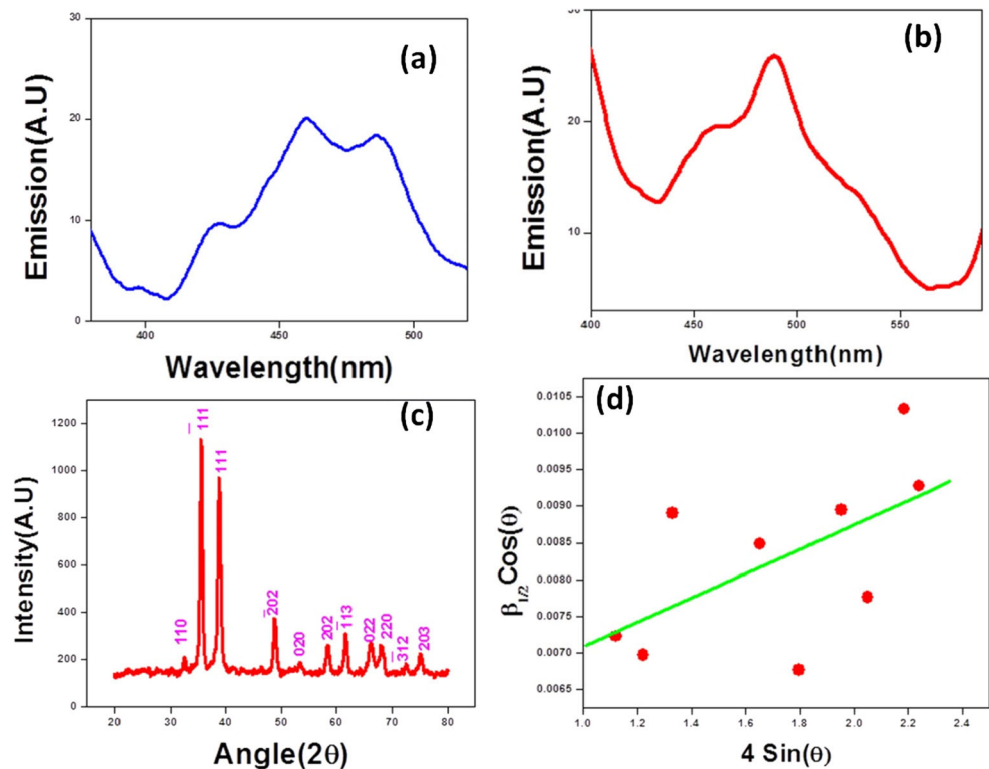
$$R_{\text{hkl}} = \frac{K\lambda}{\beta \cos\theta}$$

Here, R_{hkl} is the crystalline size and $K = 0.94$, for copper radiation. The average particle size from this equation is found to be ~ 17.88 nm. The strain (ϵ) and grain size (D) of the nanomaterial is also calculated using the Williamson-Hall (W-H) equation [37]:

$$\beta \cos\theta = \frac{k\lambda}{D} + 4\epsilon \sin\theta$$

The average size (D) and dislocation density $d = 1/D^2$ are calculated [35]. The average crystal size of CuO NPs is found

Fig. 2 **a** Emission spectrum of CuO NPs with excitation wavelength 320 nm. **b** Emission spectrum of CuO NPs with excitation wavelength 340 nm. **c** XRD spectrum of CuO NPs. **d** Plot of $\beta_{1/2}\cos\theta$ vs. $4\sin\theta$ of CuO NPs sample



to be 17.88 nm from the Scherrer formula and 22.73 nm from the fitted result of the W-H equation (Fig. 2d). The value of strain is 0.00166 from the fitted result of the W-H equation and 0.0052 from Scherrer equation. The value of dislocation density is $3.127 \times 10^{-3}/\text{nm}^2$ from the result of the W-H and $1.928 \times 10^{-3}/\text{nm}^2$ from the Scherrer equation. The calculated lattice parameters are $a = 4.568 \text{ \AA}$, $b = 3.4451 \text{ \AA}$, and $c = 5.211 \text{ \AA}$ [38].

3.5 Concentration-Dependent Absorption Spectrum of CuO-BSA Bioconjugates

The absorption spectrum of CuO NPs–BSA bioconjugate is shown in Fig. 3. The phenyl group of Tryptophan (Trp) and Tyrosin (Tyr) residues inside BSA molecule produce a maximum absorbance of around $\sim 278 \text{ nm}$ (shown in Fig. 3a (a)) [39]. The absorbance at 278 nm of the BSA increases as the concentration of the CuO NPs increases within the CuO-BSA bioconjugate. Here, we use the concentration range of CuO NPs from $12.5 \mu\text{M}$ to $113.13 \mu\text{M}$, noted as small concentration

range. The maximum peak height of the free BSA ($\sim 278 \text{ nm}$) broadens and significantly reduces from its original peak height (Fig. 3a) after the addition of CuO NPs within this range of concentration. The shape of the peak around $\sim 278 \text{ nm}$ for free BSA also changes after the addition of CuO nanoparticles within the bioconjugate (Fig. 3a). The maximum absorbance peak (at $\approx 385.25 \text{ nm}$) for CuO nanoparticles also increases within the bioconjugate. The total absorbance of the CuO NPs–BSA system increases due to the formation of the ground state complex [40]. We use another set of concentration range from $125.71 \mu\text{M}$ to $1257.16 \mu\text{M}$, called large concentration range. The use of the large concentration of the CuO NPs (Fig. 3c) suppressed the protein absorbance peak at 278 nm and CuO NPs absorbance arises significantly. The Trp peak of BSA at 278 nm is suppressed by the large amount of dosages. This may be due to the larger concentration of the CuO NPs which leads to a smaller amount of protein molecules on its surface [41]. The overlay plot of the absorption spectrum of pure CuO NPs, pure BSA, and BSA–CuO NPs bioconjugate is shown in Figure S4 (see supplementary S6). We observe a maximum

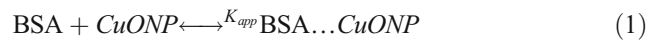
Table 1 Characterization parameters from optical study of CuO NPs

Absorption spectrum			Emission spectrum		
λ_{max}	E_g	E_U	λ_{ext}	λ_{em}	Energy
385.25 nm	3.60 eV	1.026 eV	340 nm	458 nm, 487.96 nm	2.72 eV, 2.55 eV
			320 nm	426 nm, 459.52 nm, 486.51 nm	2.92 eV, 2.71 eV, 2.56 eV

Table 2 Characterization parameters from XRD of CuO NPs

X-ray diffraction					
Size of the CuO NPs			Lattice parameters		
Scherrer formula	W-H equation	Average size	a (Å ⁰)	b (Å ⁰)	c (Å ⁰)
17.88 nm	22.73 nm	20.31 nm	4.568	3.4451	5.211

red shifting of ~ 5 nm and ~ 8 nm for the absorbance of the BSA corresponding the use of the small concentration and large concentration of the CuO NPs. This red shifting of the BSA peak is due to the energy transfer between CuO NPs to BSA molecules. The significant increment within the absorbance intensity at the wavelength of 278 nm is observed. The increment of the CuO nanoparticles concentration leads to spreading of the peptide chains of BSA and advances the exposure of Trp and Tyr residues [42]. The equilibrium for the bioconjugate formation of CuO NPs–BSA complex is given by:



The value of the association constant (K_{app}) was calculated from the Benesi and Hildebrand method [43, 44] (see supplementary S3):

$$\frac{1}{A_{obs} - A_0} = \frac{1}{A_c - A_0} + \frac{1}{K_{app}(A_c - A_0)[Q]} \tag{2}$$

where $[Q]$ is the concentration of CuO NPs. The variation of $1/(A_{obs} - A_0)$ versus $1/[Q]$ corresponding to the use of two different set concentration ranges is shown in Fig. 3b, d. The linear fitting is done by the origin 7 software by using this data. The slop of the linear fitting gives $1/K_{app}(A_c - A_0)$ and an intercept adequate to $1/(A_c - A_0)$ (Fig. 3b, d). The value of K_{app} is found to be $6.51 \times 10^3 M^{-1}$ and $2.16 \times 10^3 M^{-1}$ for the small concentration range and large concentration range, respectively. The three times greater value of the apparent association constant in the low

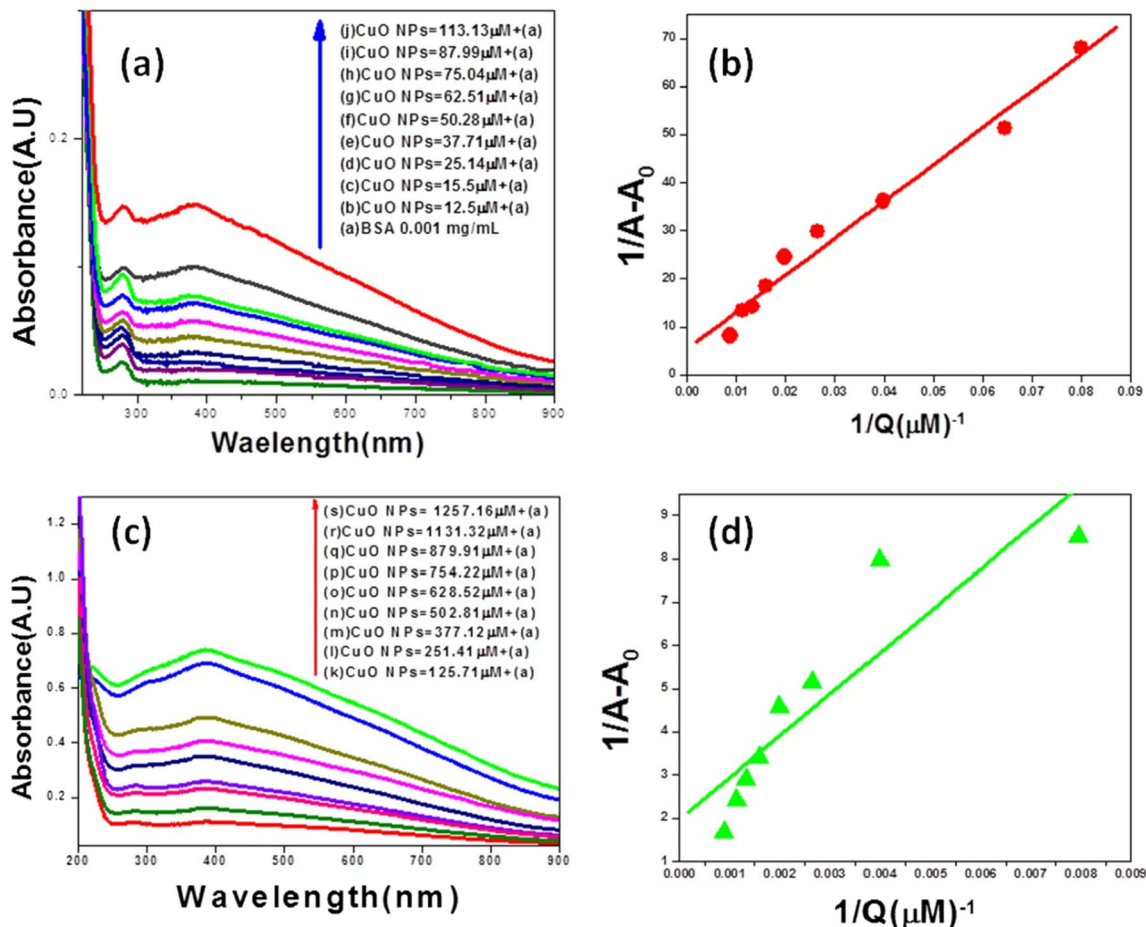


Fig. 3 a Absorption spectra of (a) BSA 0.001 mg/mL, (b) CuO 12.5 μM + BSA, (c) CuO 15.5 μM + BSA, (d) CuO 25.14 μM + BSA, (e) CuO 37.71 μM + BSA, (f) CuO 50.28 μM + BSA, (g) CuO 62.51 μM + BSA, (h) CuO 75.04 μM + BSA, (i) CuO 87.99 μM + BSA, (j) CuO 113.13 μM + BSA. b Plot of $1/(A - A_0)$ vs. $1/Q$ in the small concentration

range. c Absorption spectra of BSA 0.01 mg/mL + (k) CuO 125.71 μM, (l) CuO 251.41 μM, (m) CuO 377.12 μM, (n) CuO 502.81 μM, (o) CuO 628.52 μM, (p) CuO 754.22 μM, (q) CuO 879.91 μM, (r) CuO 1131.32 μM, (s) CuO 1257.16 μM. d Plot of $1/(A - A_0)$ vs. $1/Q$ in the large concentration range

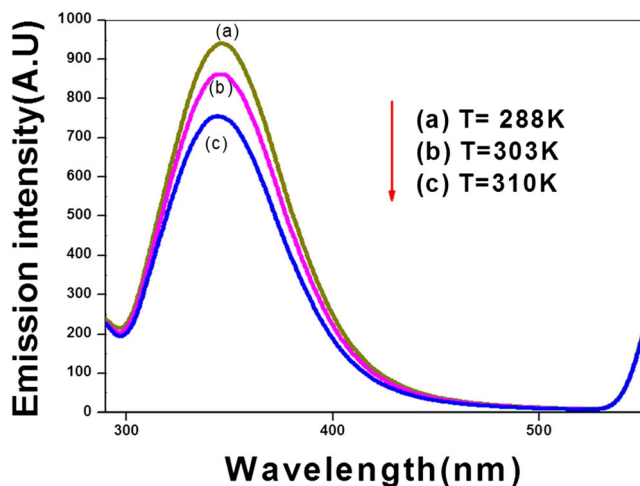


Fig. 4 Emission spectrum of pure BSA protein at the temperature (a) $T = 288$ K, (b) $T = 303$ K, and (c) $T = 310$ K

concentration region supporting the large amount of protein on the CuO NPs surfaces leads to a strong protein–CuO NPs complex formation in the ground state than that in the large concentration region.

3.6 Time-Dependent Energy Transfer Between CuO NPs and BSA with Different Dosages of CuO NPs Under Heat Treatment from Steady-State Fluorescence Spectroscopy

The emission intensity of free BSA changes dynamically with respect to time after bioconjugation with CuO nanoparticles (Fig. 5). We studied this dynamic emission changes under heat treatment by tuning the temperature from 288 to 310 K. The observed decrease in the emission intensity corresponding to each temperature is a signature of energy transfer mechanism. The energy transfer efficiency (E_{eff}) due to dynamic energy changes between CuO NPs and BSA within the CuO NPs–BSA bioconjugate is calculated and analyzed by considering dipole-dipole coupling from the following formula [44, 45]:

$$E_{\text{eff}} = 1 - \frac{I}{I_0} \quad (3)$$

Here, I_0 is the emission intensity of free BSA and I is the emission intensity of BSA within the BSA–CuO NPs bioconjugate. The free BSA emission at room temperature is shown

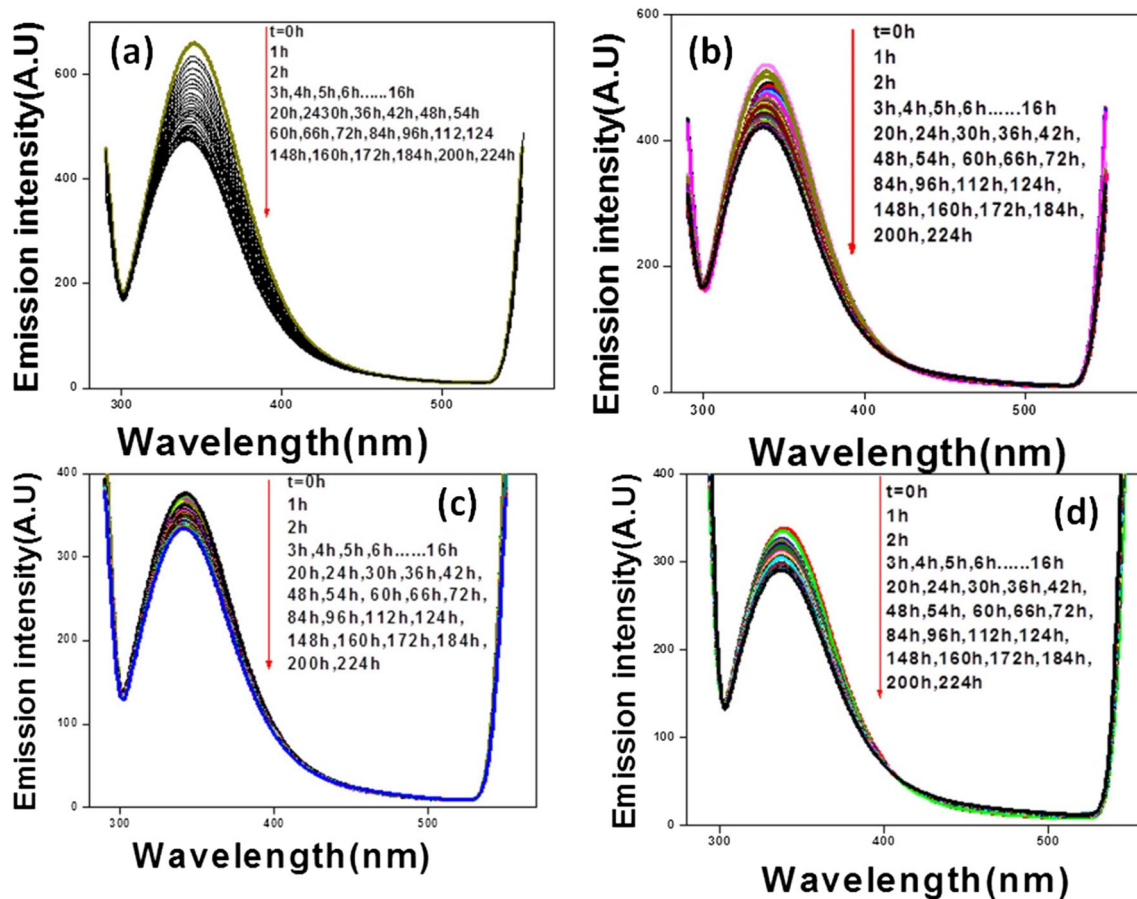


Fig. 5 Emission of BSA–CuO NPs bioconjugate **a** with BSA = 0.001 mg/mL and CuO NPs = 25.14 μM under different time (0 to 224 h) at room temperature 298 K, **b** with BSA = 0.001 mg/mL and CuO NPs = 25.14 μM under different time (0 to 224 h) at body temperature 310 K, **c**

with BSA = 0.001 mg/mL and CuO NPs = 378 μM under different time (0 to 224 h) at room temperature 298 K, and **d** with BSA = 0.001 mg/mL and CuO NPs = 378 μM under different time (0 to 224 h) at body temperature 310 K

in Fig. 4a. Figure 5 shows the emission spectra of BSA ($C_{0.001}$ mg/mL) within the CuO NPs–BSA bioconjugate under different time from associate initial condition of the bioconjugate formation. The variation of room temperature emission and energy transfer efficiency (E_{eff}) with time of the CuO NPs–BSA bioconjugates ($Q_{[\text{CuO NPs}]} = 25.14 \mu\text{M}$) are shown in Figs. 6a and 7a, respectively. The result shows that the dynamic change within the emission intensity falls rapidly as much as up to 34 h because of the quick rate change of energy transfer efficiency (E_{eff}); after 34 h, it goes towards a steady state as a result of the steady rate of energy transfer efficiency. Upon binding on the CuO NP surface, the emission intensity of BSA quenched with time, with a slight red shift. The energy transfer occurs due to Trp and Tyr residues present in the BSA structure because BSA is formed of three homologous domains (I, II, III) that contain twenty Tyr residues and two Trp residues [46] (for details, see supplementary S4& S5). The structure of BSA under different views (atoms, bonding, % (insertion code)s, atomic balls) is shown in Fig. 8. The partial diminish in emission of tryptophan (at 340 nm) intensity within the presence of CuO NPs is feasible once the tertiary deformation of adsorbed BSA molecules is altered in such a simplest way that the Trp moieties involve locations within the

shut closeness of other fluorescence quenching amino acids [47]. Here, the quenching of the emission intensity of tryptophan attains a steady state after 34 h and ultimately closely saturation arises (spectra from 34–224 h). This indicates that upon preliminary binding on CuO nanoparticle surface, BSA molecules receives tertiary deformation, i.e., a partial loss in its tertiary conformation, and failed to endure forceful conformational changes. At the body temperature, the emission intensity of free BSA falling rapidly up to 24 h (Fig. 6b) in the presence of CuO NP with a quick rate of energy transfer efficiency (E_{eff}), after 24 h it goes about steady state and rate of energy transfer slows down into saturation value (Fig. 7b). In the case of using the large concentration of the CuO NPs ($378 \mu\text{M}$), the steady-state (towards) emission of the bioconjugate occurs beyond 45 h and 36 h at room temperature and body temperature, respectively (Fig. 6c and d, respectively). In the small concentration region, the saturated value of E_{eff} around 45% occurs within 224 h. This value is almost the same as the room temperature and human normal body temperature. The change in E_{eff} at room temperature is from 23.4 to 45.4%, i.e., $\Delta E_{\text{eff}} = 22\%$, and at body temperature is from 30.6 to 44%, i.e., $\Delta E_{\text{eff}} = 13.6\%$. When we use large concentration,

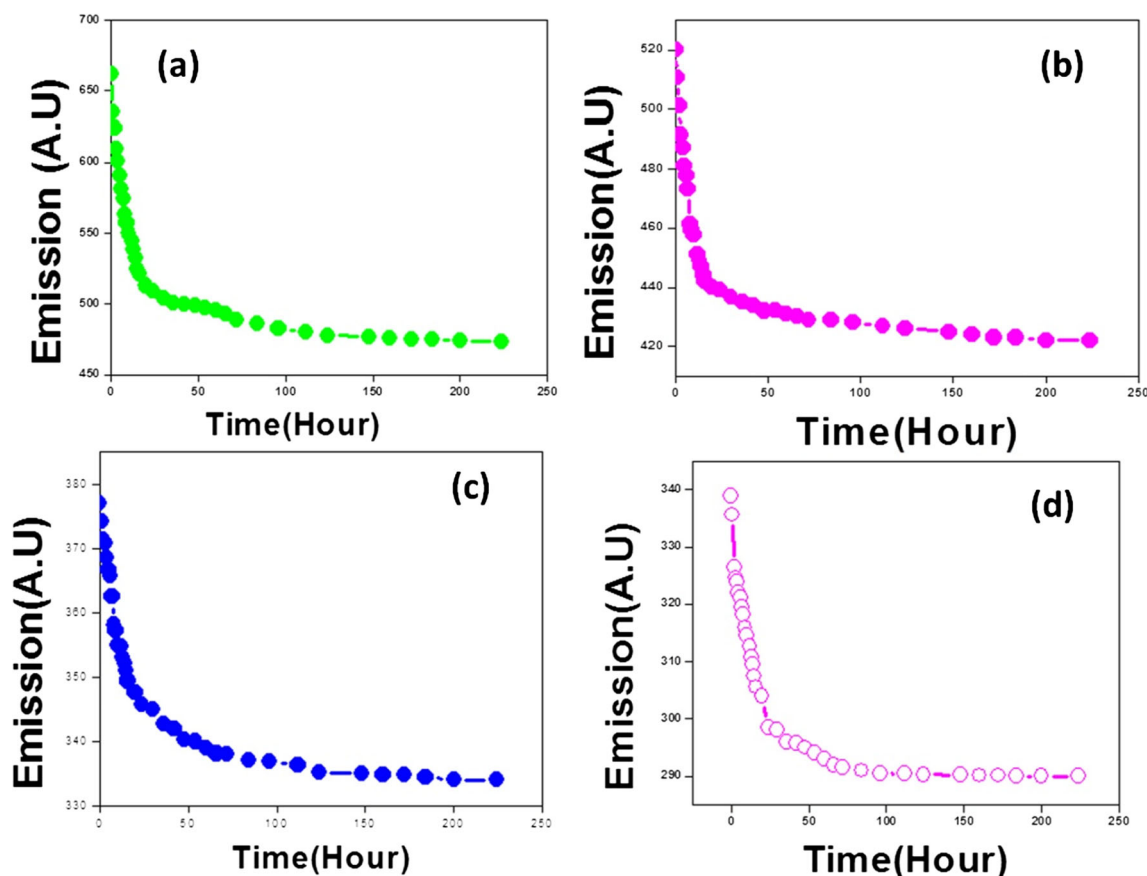


Fig. 6 Variation of emission intensity with time of the bio conjugate. **a** BSA = 0.001 mg/mL and CuO NPs = 25.14 μM under at room temperature 298 K. **b** BSA = 0.001 mg/mL and CuO NPs = 25.14 μM at body

temperature 310 K. **c** BSA = 0.001 mg/mL and CuO NPs = 378 μM at room temperature 298 K. **d** BSA = 0.001 mg/mL and CuO NPs = 378 μM at body temperature 310 K

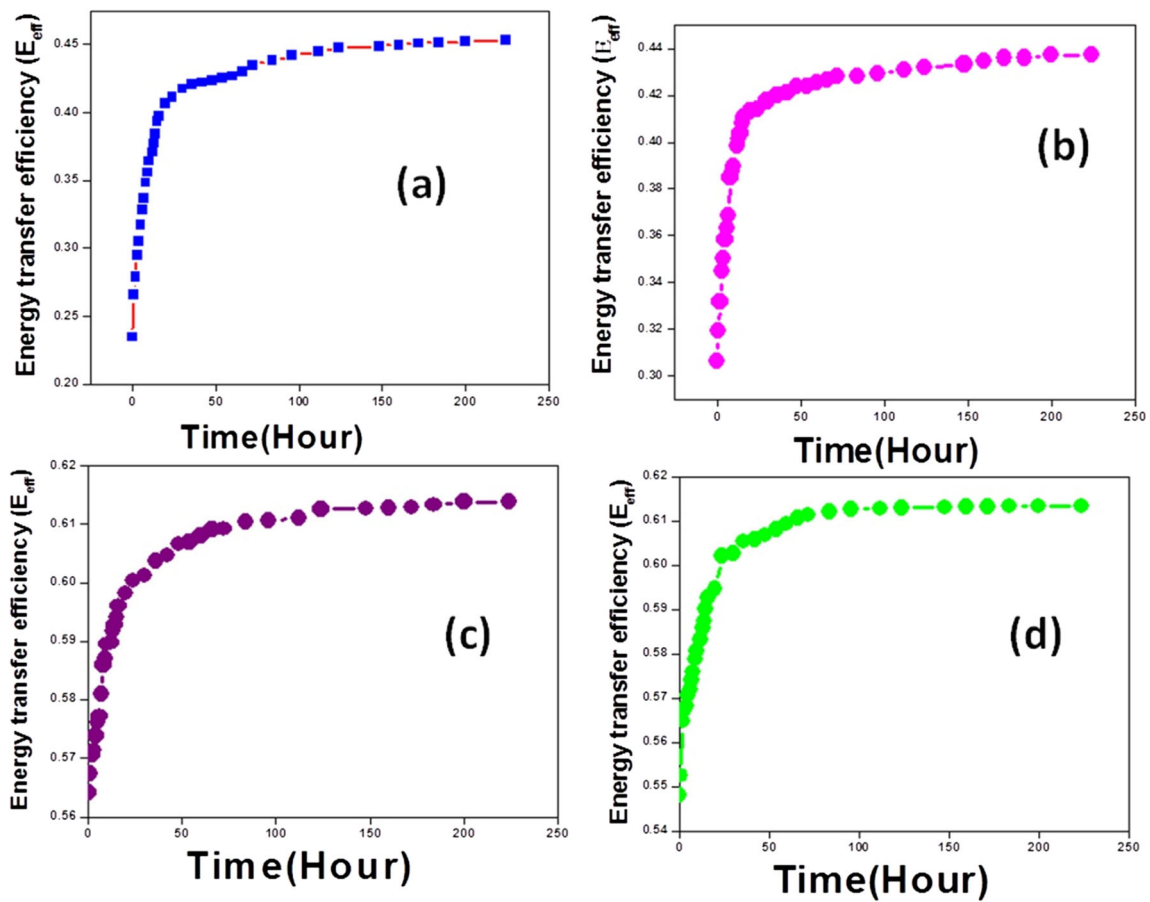
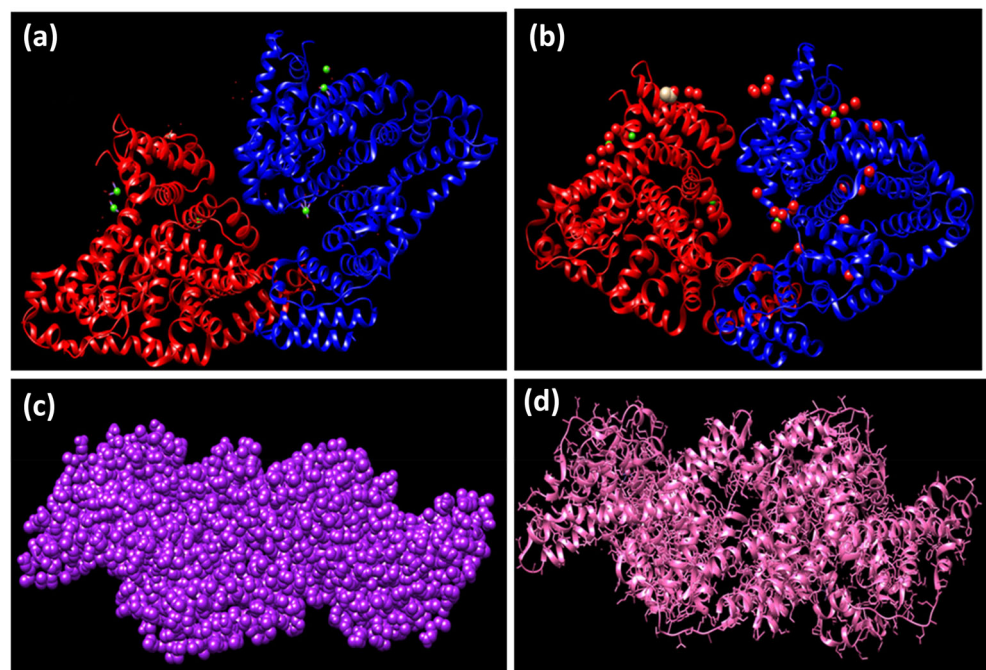


Fig. 7 Variation of the energy transfer efficiency (E_{eff}) with time of the bio conjugate. **a** BSA = 0.001 mg/mL and CuO NPs = 25.14 μM under at room temperature 298 K. **b** BSA = 0.001 mg/mL and CuO NPs =

25.14 μM at body temperature 310 K. **c** BSA = 0.001 mg/mL and CuO NPs = 378 μM at room temperature 298 K. **d** BSA = 0.001 mg/mL and CuO NPs = 378 μM at body temperature 310 K

Fig. 8 Structure of BSA. **a** %(Insertion code)s. **b** %(Atoms), **c** %(Atoms)_Sphere. **d** Bonds



a large amount of energy transfer occurs initially due to a large amount of the quencher (CuO NPs), but the rate of energy transfer is slow. Within 224 h, the E_{eff} changes from 54.4 to 62% at room temperature and that from 54.8 to 61.4% of body temperature. The total change (ΔE_{eff}) is 5.6% at room temperature and 6.6% at body temperature. Hence, the total change in energy transfer within 224 h is almost 6% for both temperatures, i.e., E_{eff} is almost independent of the temperature for a large concentration of the quencher. In small concentration region, E_{eff} depends on the temperature, whereas in large concentration regions, E_{eff} is almost independent of the temperature. Energy transfer strongly depends on the concentration of the CuO NPs used.

3.7 Emission of CuO NPs–BSA Bioconjugate Under Heat Treatment: Fluorescence Quenching Study With Small and Large Concentration Range

We studied the change in the emission spectrum of the pure BSA molecule for the use of small concentration and large concentration range of the CuO NPs under heat treatment (Figs. 9 and 11, respectively). The emission of pure BSA protein at the three different temperatures (288 K, 300 K, 311 K) is shown in Fig. 4. The maximum intensity of free BSA at 340 nm decreases with an increase in temperature due to heat inducing changes within the BSA structure. The maximum emission peak at 340 nm of the BSA due to Trp is

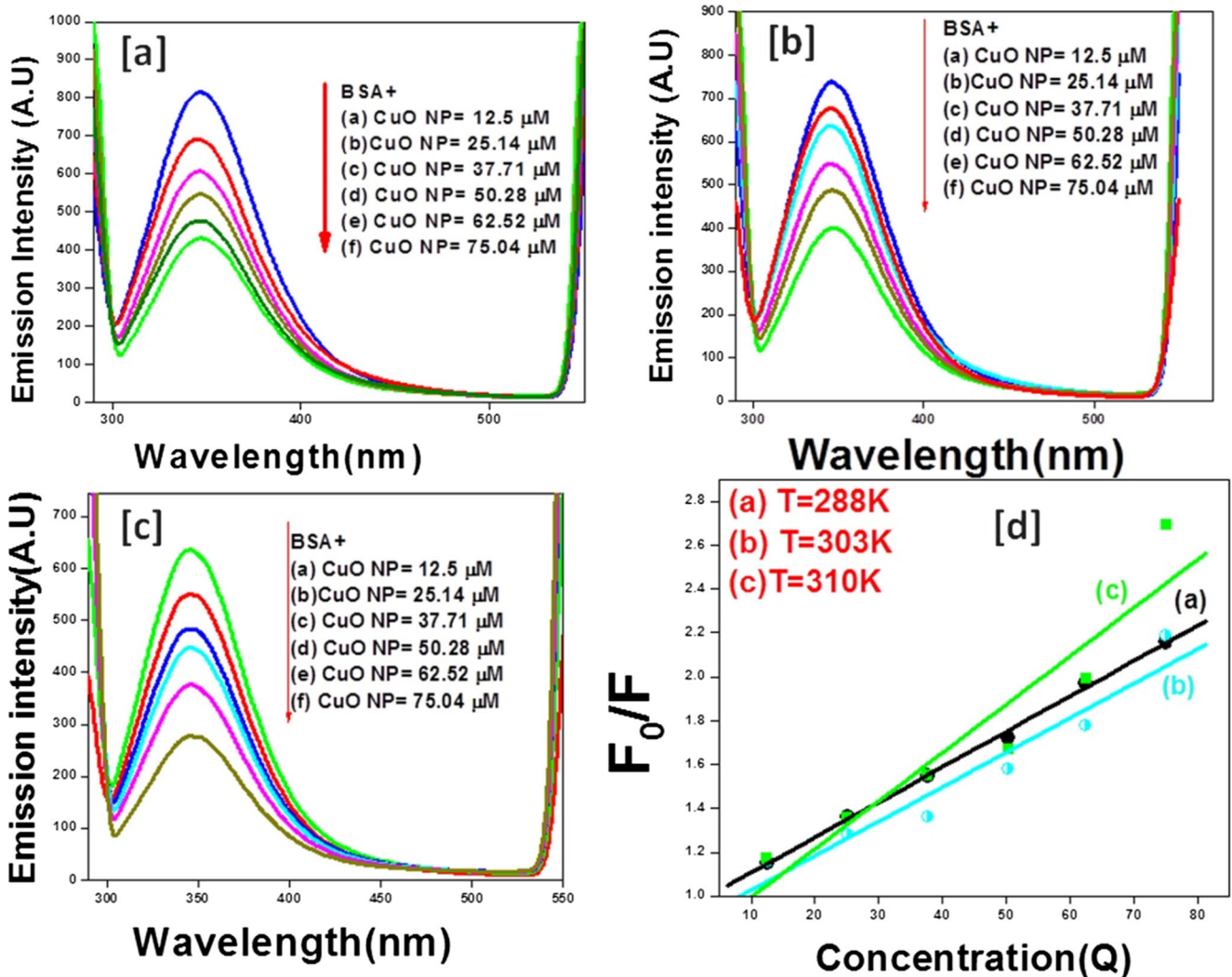


Fig. 9 a Represents the fluorescence spectrum of CuO NPs–BSA bioconjugate at 288 K with $C_{\text{BSA}} = 0.001$ mg/mL + (a) $Q_{\text{CuO}} = 12.5$ μM , (b) $Q_{\text{CuO}} = 25.14$ μM , (c) $Q_{\text{CuO}} = 37.71$ μM , (d) $Q_{\text{CuO}} = 50.28$ μM , (e) $Q_{\text{CuO}} = 62.52$ μM , (f) $Q_{\text{CuO}} = 75.04$ μM . **b** Fluorescence spectrum of CuO NPs–BSA bioconjugate at 303 K with $C_{\text{BSA}} = 0.001$ mg/mL + (a) $Q_{\text{CuO}} = 12.5$ μM , (b) $Q_{\text{CuO}} = 25.14$ μM , (c) $Q_{\text{CuO}} = 37.71$ μM , (d) $Q_{\text{CuO}} = 50.28$ μM , (e) $Q_{\text{CuO}} = 62.52$ μM , (f) $Q_{\text{CuO}} = 75.04$ μM . **c** Fluorescence

spectrum of CuO NPs–BSA bioconjugate at 310 K with $C_{\text{BSA}} = 0.001$ mg/mL + (a) $Q_{\text{CuO}} = 12.5$ μM , (b) $Q_{\text{CuO}} = 25.14$ μM , (c) $Q_{\text{CuO}} = 37.71$ μM , (d) $Q_{\text{CuO}} = 50.28$ μM , (e) $Q_{\text{CuO}} = 62.52$ μM , (f) $Q_{\text{CuO}} = 75.04$ μM . **d** Variation of F_0/F versus Q plot for CuO NPs–BSA complex at the temperatures (a) 288 K, (b) 303 K, and (c) 310 K in the low-concentration range

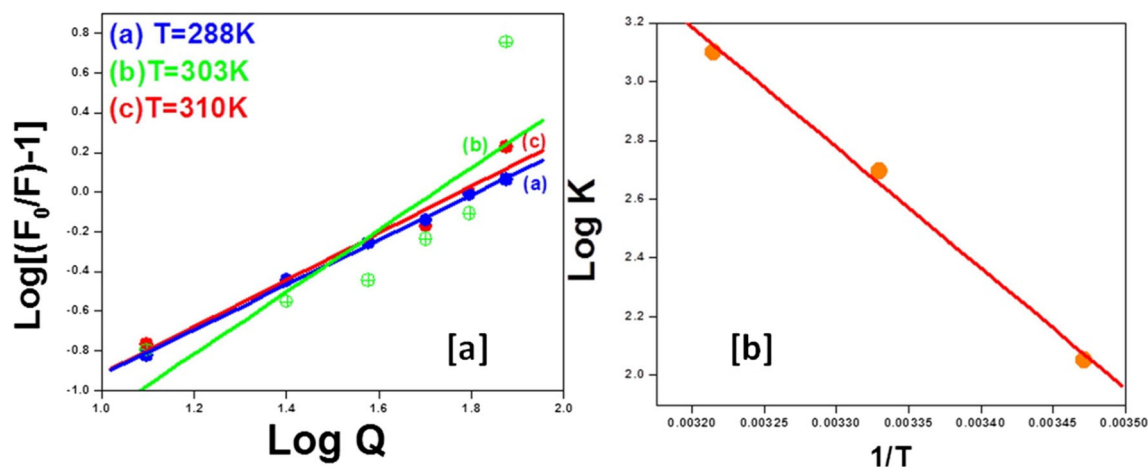


Fig. 10 **a** Represents the $\log[(F_0/F) - 1]$ versus $\log[Q]$ plot for CuO NPs–BSA complex at the temperatures (a) 288 K, (b) 303 K, and (c) 310 K in the low-concentration range. **b** Variation of $\log K$ versus $1/T$ plot for CuO NPs–BSA complex in the low-concentration range

modified by the addition of CuO NPs of various concentrations ($Q_{\text{CuO}} = 12.5$ to $75.04 \mu\text{M}$) under three different temperatures (288 K, 300 K, 311 K). In size modification, the intensity reduces with red shifting in the pure BSA fluorescence spectrum under the addition of different CuO NP concentrations suggesting the prevalence of the fluorescence quenching process (Fig. 9a, b, c) [48]. Red shift of ~ 2 nm is found with $Q_{\text{CuO}} = 75.04 \mu\text{M}$ and $C_{\text{BSA}} = 0.001$ mg/mL owing to raising hydrophobicity caused by CuO NPs [49]. The binding of CuO NPs with BSA is studied by the documented Stern-Volmer (S-V) equation [50, 51]

$$\frac{F_0}{F} = K_{\text{SV}}[Q] + 1 \quad (4)$$

Here F_0 and F are the steady-state emission intensities of BSA within the absence and presence of CuO NPs, respectively, and Q is the concentration of CuO NPs. The values of S-V quenching constant (K_{SV}) for 288 K, 300 K, and 311 K temperatures are summarized in Table 3. Here, we observed the decrement of K_{SV} with increment of temperature from 288 to 300 K which indicates that the quenching mechanism of BSA is a static for the use of low concentration of the CuO NPs, and therefore, the strength of interaction decreases inside this varying temperature [53]. Inside the temperature (T) range 300 to 311 K, we observe the increment of K_{SV} with T signifying that the quenching mechanism of BSA could be a dynamic quenching process in the presence of CuO NPs. Hence,

the strength of interaction increases inside these T variations [54]. The observed quenching is a mixed kind, i.e., each dynamic and static quenching is present under a low concentration range of the CuO NPs [40]. The F_0/F versus $[Q]$ plots at different temperature are shown in Fig. 9d. (For details of conditions regarding static and dynamic quenching see our previous reports [40, 52].)

The emission of BSA–CuO NPs bioconjugate within the large concentration range of the CuO NPs are shown in Fig. 11a, b, c for the temperatures 288 K, 303 K, and 310 K, respectively. The maximum emission peak (340 nm) of the pure BSA is largely modified within the shape and size for such concentration range and the corresponding red shifting is 5 nm. The fluorescence quenching of BSA protein is large under a large concentration range compared with the use of the small concentration range for any particular temperature. Larger protein quenching leads to large protein denaturation with leading energy transfer between a large concentration of CuO NPs and BSA protein. The F_0/F vs. $[Q]$ plots at different temperatures within the large concentration range are shown in Fig. 11d.

In the large amount of the dosages of CuO NPs, the value of K_{SV} gently increases with the increase of the temperature from 288 to 311 K (Table 4) signifying that the quenching mechanism is a dynamic nature in the presence of high dosages of CuO NPs and the strength of interaction increases in this varying temperature [55, 56]. The binding constant K and the number of binding sites (n) between BSA and CuO NPs at

Table 3 Binding parameters and thermodynamic parameters of BSA–CuO Nanoparticle interactions. Small-concentration range CuO NPs

T (K)	K_{SV} (M^{-1})	$\text{Mod}(\log K)$ (μM) $^{-1}$	ΔG° (kJ/mol)	ΔH° (kJ/mol)	ΔS° (J/mol)	n
288 K	182.2	2.052	− 4.911	− 35.638	135.467	1.15
303 K	156.9	2.697	− 6.726			1.32
310 K	219.5	3.099	− 8.0138			1.51

Table 4 Binding parameters and thermodynamic parameters of BSA–CuO Nanoparticle interactions. Large-concentration range of CuO NPs

<i>T</i> (K)	<i>K</i> _{SV} (M ⁻¹)	Mod(log <i>K</i>) (μM ⁻¹)	Δ <i>G</i> ^o (kJ/mol)	Δ <i>H</i> ^o (kJ/mol)	Δ <i>S</i> ^o (J/mol)	<i>n</i>
288 K	8.43	0.815	− 1.95	− 13.95	− 54.53	0.49
303 K	24.13	0.9549	− 2.394			0.62
310 K	50.4	1.25	−3.231			0.71

different temperatures with different range of concentrations are calculated using the below equation [54]:

$$\log \left[\frac{F_0}{F} - 1 \right] = \log K + n \log [Q] \tag{5}$$

The variation of $\log[\frac{F_0}{F} - 1]$ vs. $\log[Q]$ is shown in Figs. 10a and 11a for the use of small concentration range and large concentration range, respectively. The values of *n* and log*K*, at 288 K, 300 K, and 311 K, are organized in Tables 3 and 4 for comparison.

The result for the number of binding sites (*n*) (see Tables 3 and 4) shows that “*n*” increases with an increase in the temperature range in both use of the lower and higher concentration range of the CuO NPs. In the case of high concentration (*Q*), the value of *n* is less than one (*n* < 1) signifying a negative cooperative reaction between CuO NPs and BSA [57, 58]. However, in the low concentration region, the value of *n* is greater than one (*n* > 1) signifying a positive cooperative reaction between CuO NPs and BSA. The large value of the binding sites (*n* > 1) in all temperatures of the lower

concentration region is due to the large amount of protein molecules in the surface supporting the absorption spectrum of the CuO-BSA bioconjugate [57, 58]. The value of *n* is small (< 1) in the high *Q* range corresponding to smaller amount of BSA molecules on its surface. The thermodynamic parameters (change in enthalpy, Δ*H*; change in Gibb’s free energy, Δ*G*; change in entropy, Δ*S*) for BSA and CuO NPs bioconjugates are calculated using the van ’t Hoff equation [59]

$$\ln K = - \frac{\Delta H}{RT} + \frac{\Delta S}{R} \tag{6}$$

The variation of log*K* vs. 1/*T* graph for CuO NPs–BSA bioconjugate is shown in Figs. 10b and 12b for the use of small concentration and large concentration range, respectively. The Gibbs free energy change is:

$$\Delta G = \Delta H - T\Delta S = -RT \ln K \tag{7}$$

The thermodynamic parameters of the CuO NPs–BSA bioconjugate are summarized in Tables 3 and 4 [59]. We

Fig. 11 **a** Represents the fluorescence spectrum of CuO NPs–BSA bio conjugate at 288 K with *C*_{BSA} = 0.001 mg/mL + (a) *Q*_{CuO} = 125.7 μM, (b) *Q*_{CuO} = 377.1 μM, (c) *Q*_{CuO} = 678.5 μM, (d) *Q*_{CuO} = 879.9 μM, (e) *Q*_{CuO} = 1131 μM, (f) *Q*_{CuO} = 1257.16 μM. **b** Fluorescence spectrum of CuO NPs–BSA bioconjugate at 303 K with *C*_{BSA} = 0.001 mg/mL + (a) *Q*_{CuO} = 125.7 μM, (b) *Q*_{CuO} = 377.1 μM, (c) *Q*_{CuO} = 678.5 μM, (d) *Q*_{CuO} = 879.9 μM, (e) *Q*_{CuO} = 1131 μM, (f) *Q*_{CuO} = 1257.16 μM. **c** Fluorescence spectrum of CuO NPs–BSA bioconjugate at 310 K with *C*_{BSA} = 0.001 mg/mL + (a) *Q*_{CuO} = 125.7 μM, (b) *Q*_{CuO} = 377.1 μM, (c) *Q*_{CuO} = 678.5 μM, (d) *Q*_{CuO} = 879.9 μM, (e) *Q*_{CuO} = 1131 μM, (f) *Q*_{CuO} = 1257.16 μM. **d** Variation of *F*₀/*F* versus *Q* plot for CuO NPs–BSA complex at the temperatures (a) 288 K, (b) 303 K, and (c) 310 K in the large-concentration range

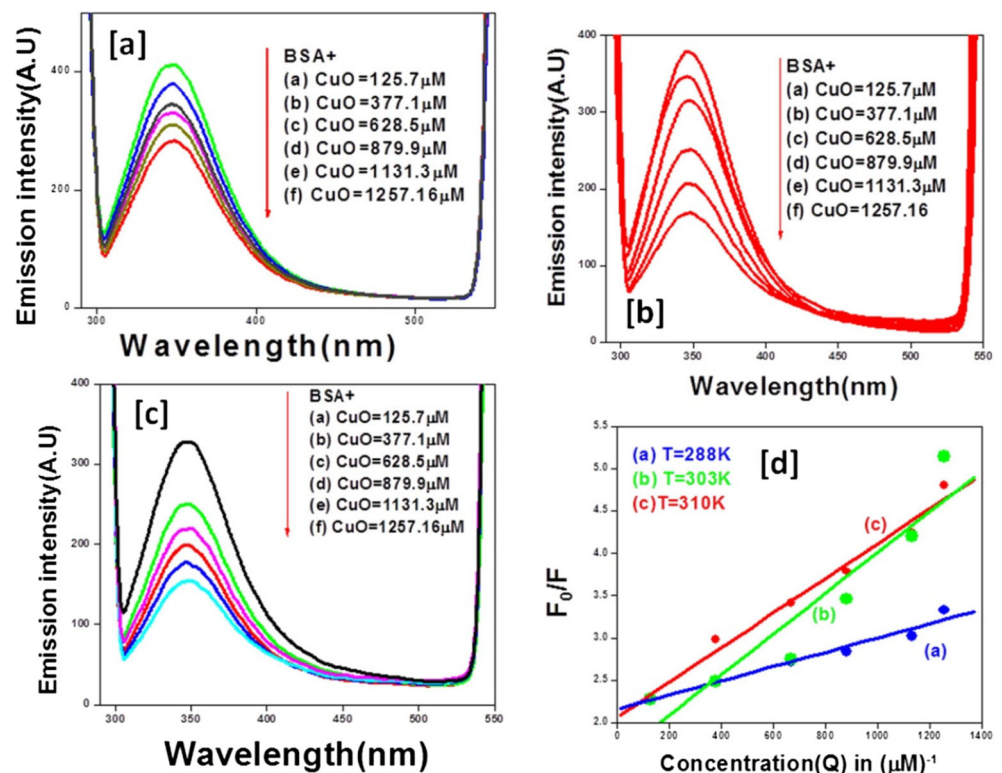
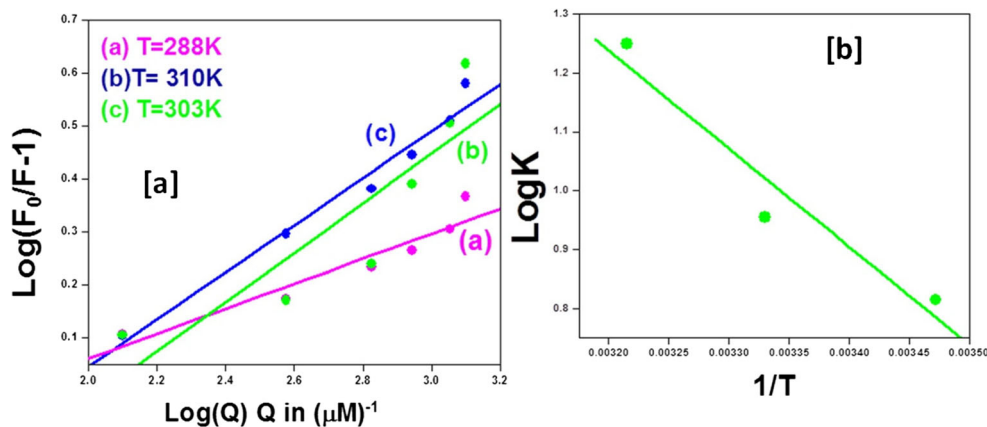


Fig. 12 **a** Represents the $\log[(F_0/F) - 1]$ versus $\log[Q]$ plot for CuO NPs–BSA complex at the temperatures (a) 288 K, (b) 303 K, and (c) 310 K in the large-concentration range. **b** Variation of $\log K$ versus $1/T$ plot for CuO NPs–BSA complex in the large-concentration range



find that in ΔG , ΔH is negative and ΔS is positive. Hence, spontaneous binding occurs in an exothermic interactive way [60–62]. The positive ΔS constitutes that electrostatic interaction is the leading force for binding the BSA on CuO NPs [63, 64]. Electrostatic binding between BSA and oxide materials were studied by Sun et al. [65]. Also, the hydrophobic interaction is present along with electrostatic interaction. The hydrophobic interaction is confirmed from red shift of the fluorescence peak of free BSA in the presence of CuO NPs. The interactive forces involved in the BSA–CuO NPs conjugate is independent of the concentration of CuO NPs used.

3.8 Time-Resolved Fluorescence on BSA–CuO NP Bioconjugate and Energy Transfer Within the Conjugate

Time-resolved fluorescence activity is a vital and sensitive technique to understand the result of the microenvironment encompassing a fluorescent molecule [66, 67]. To determine the origin and efficiency of the energy transfer between BSA and CuO NPs, excited-state lifetimes of BSA and BSA–CuO NPs bioconjugate were measured by time-resolved fluorescence spectroscopy. Measurements were performed for free BSA and so upon the addition of CuO NPs to the BSA solution. We have measured the fluorescence lifetime of BSA protein within the CuO NPs–BSA bioconjugate (Fig. 13). The decay curve of free BSA was fitted bi-exponential with lifetimes of 3.26 ns and 6.61 ns (see Table 5). Recent studies have shown that the shorter lifetime is freelance of any structure and is characterized as an interior property and organization of the tryptophan structure within the excited state [68]. We consider the average value of lifetime instead of individual component. The calculated average lifetime is 4.94 ns for free BSA molecule. The fluorescence lifetime of BSA was found to have decreased in the presence of CuO nanoparticles (see Fig. 13) as shown in

Table 5. This was presumably due to energy transfer from the adsorbed protein to the CuO nanoparticle. The lifetime results clearly concluded that the quenching of fluorescence in the presence of CuO NPs is dynamic in nature.

The energy transfer efficiency (φ_{ET}), that is that the fraction of photons absorbed by the donor that are transferred to acceptor, will be determined from the PL lifetimes according to the bellow equation [69, 70]:

$$\varphi_{\text{ET}} = 1 - \tau_2 / \tau_1$$

where τ_1 and τ_2 are the lifetime of the free BSA protein and adsorbed BSA protein within BSA–CuO NP bioconjugates, respectively. The calculated energy transfer efficiency is 79.35% for the bioconjugate. The calculated φ_{ET} is greater than 70% ($\varphi_{\text{ET}} > 70\%$) which confirms that the Förster resonance energy transfer (FRET) mechanism is the key of energy transfer mechanism within the bioconjugate. A schematic representation of FRET mechanism between BSA and CuO NPs is shown in Fig. 16a.

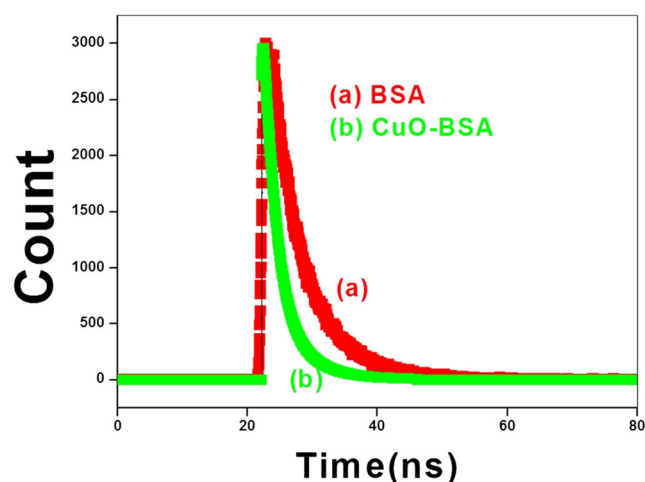


Fig. 13 The kinetic of the fluorescence decays (TCSPA) of (a) pure BSA (0.001 mg/mL) and (b) BSA + CuO NPs bioconjugate

Table 5 Lifetime from time-resolved fluorescence measurement

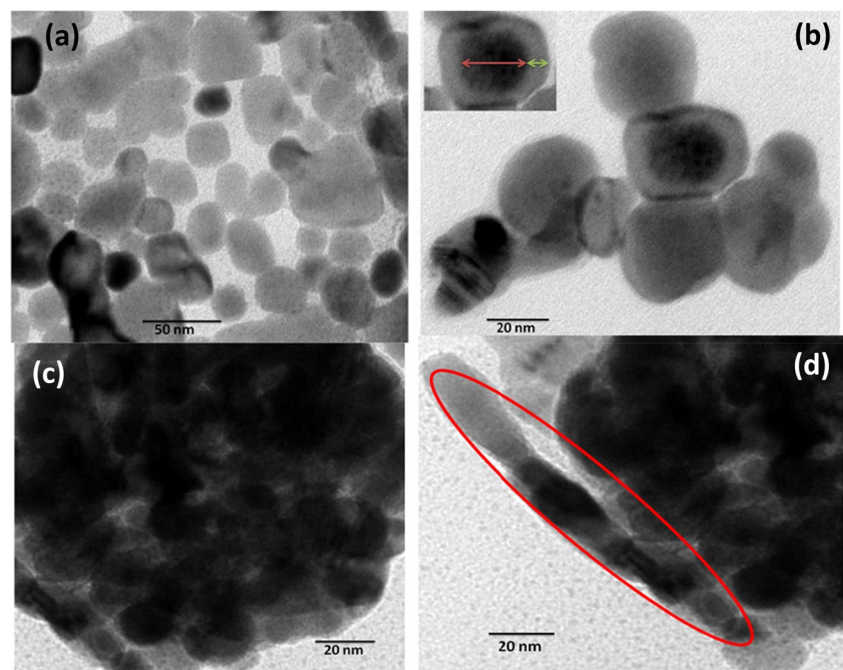
Solution	Lifetime 1	Lifetime 2	Average lifetime (τ)	Energy transfer efficiency
BSA	3.26 ns	6.61 ns	$\tau_1 = 4.94$	79.35%
BSA–CuO	0.52 ns	1.51 ns	$\tau_2 = 1.02$	

3.9 Transmission Electron Microscopy and Dynamic Light Scattering of the CuO NPs–BSA Bioconjugate

TEM or HRTEM images in Fig. 14 clearly show that nanoparticles are surrounded by protein molecules by the formation of corona in the bioconjugate. Here, BSA molecules formed corona on the surface of CuO NPs within the bioconjugate. Figure 14 shows the direct confirmation of the formation of BSA–CuO NPs corona. The clear image of the individual corona clearly observes from the TEM images for small concentration of the CuO NPs. The outer layer of BSA is bound to the formation of the corona. The magnified image of corona represents that almost spherical CuO NPs with diameter 20 nm are strongly attached with BSA (Fig. 14b). Inset of Fig. 14b shows the zoom part of the image of a corona. This image clearly represents that the core CuO NPs are fully surrounded with BSA along with a shell thickness of ~ 8 nm. This shell thickness of the BSA layer is equal with the dimension of BSA monomer (8 nm) [71]. The individual corona formation is investigated from DLS measurements. The average hydrodynamic size of the protein corona in DLS for the dosages of 12.5 μM CuO NPs is \sim

12 nm, which is slightly greater than BSA monomer (Fig. 15). This slight greater value of the corona arises due to hydrodynamic size. Hence, DLS also supports the TEM results of the corona size. The use for large concentration of CuO NPs destroyed the single corona formation mechanism. Aggregation of the CuO NPs inside the BSA molecule matrix occurs for the use of the large concentration of CuO NPs within the CuO NPs–BSA bioconjugate. This aggregation was clearly observed from the TEM images. The spherical CuO NPs are attached one by one and formed a chain-like structure inside the BSA molecules matrix (Fig. 14d). Hence, selectively single corona formation for large doses is destroyed and the tendency of the aggregation of the BSA molecules and CuO NPs is prominent. As the concentration of the CuO NPs increases, the tendency of clustering increases, and hence, the hydrodynamic radius of the CuO NPs–BSA bioconjugates increases (see Fig. 15a (b), (c), (d)). Adding 0.001 mg/mL BSA at room temperature with 12.5 μM CuO nanoparticles (Fig. 15a (a)), the particle size distribution (PSD) of the CuO NPs–BSA bioconjugate shows the near-monodispersed nature with small broadening. This broadening is large for the use of 50.28 μM CuO NPs (Fig. 15a

Fig. 14 TEM image of the CuO NPs–BSA bioconjugate. **a, b** BSA = 0.001 m/mL + CuO NP = 24.14 μM . **c, d** BSA = 0.001 m/mL + CuO NP = 378 μM



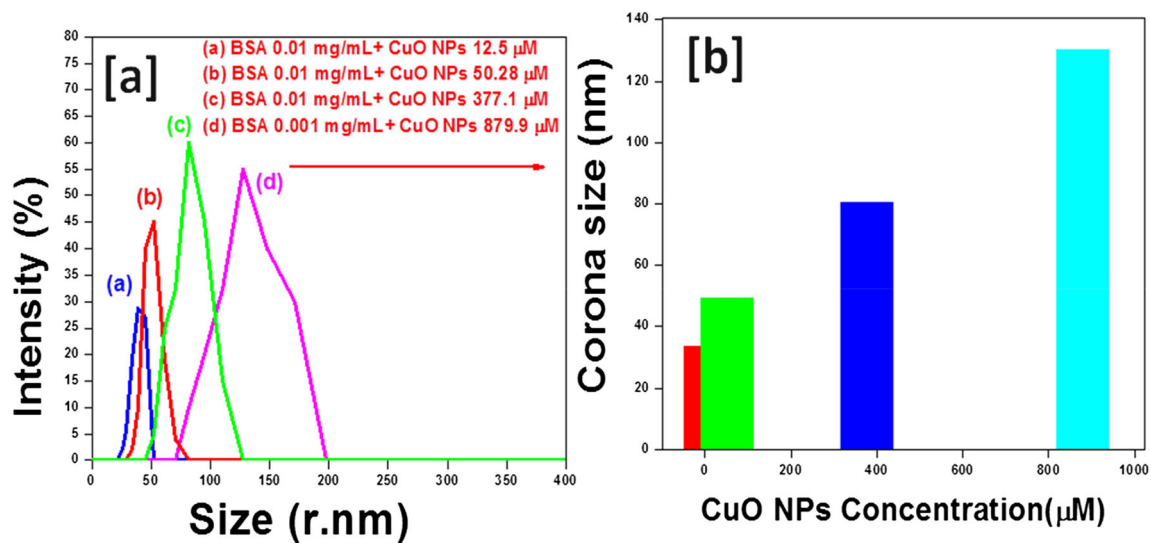


Fig. 15 **a** DLS spectra of CuO NPs–BSA bioconjugate with (a) BSA = 0.001 mg/mL + CuO NPs = 12.5 μM, (b) BSA = 0.001 mg/mL + CuO NPs = 50.28 μM, (c) BSA = 0.001 mg/mL + CuO NPs = 377.1 μM, and

(d) BSA = 0.001 mg/mL + CuO NPs = 879.9 μM. **b** Variation of the corona size with concentration of CuO NPs

(b)). This broadening is mainly due to corona formation within the bioconjugate around the single CuO nanoparticle. Hence, a small concentration dose is responsible for selective corona formation. The average hydrodynamic diameter (D_h) of the bioconjugate is 33 nm and 49 nm for the use of 12.5 μM and 50.28 μM doses, respectively. The D_h value and broadening of the PSD increases from 49 to 80 nm with an increasing use of 377.1 μM doses (Fig. 15a). This indicates the formation of few protein

aggregations leads to the tendency of nanoparticle agglomeration. Two extra peaks and large broadening of the PSD for the use of 879.9 μM CuO NPs show that the addition of BSA with this concentration of CuO NPs causes the formation large BSA aggregation around single CuO NPs, and the tendency of nanoparticle agglomeration is large. Schematic diagram of CuO nanoparticle exposure concentration effect on BSA protein adsorption is shown in Fig. 16b.

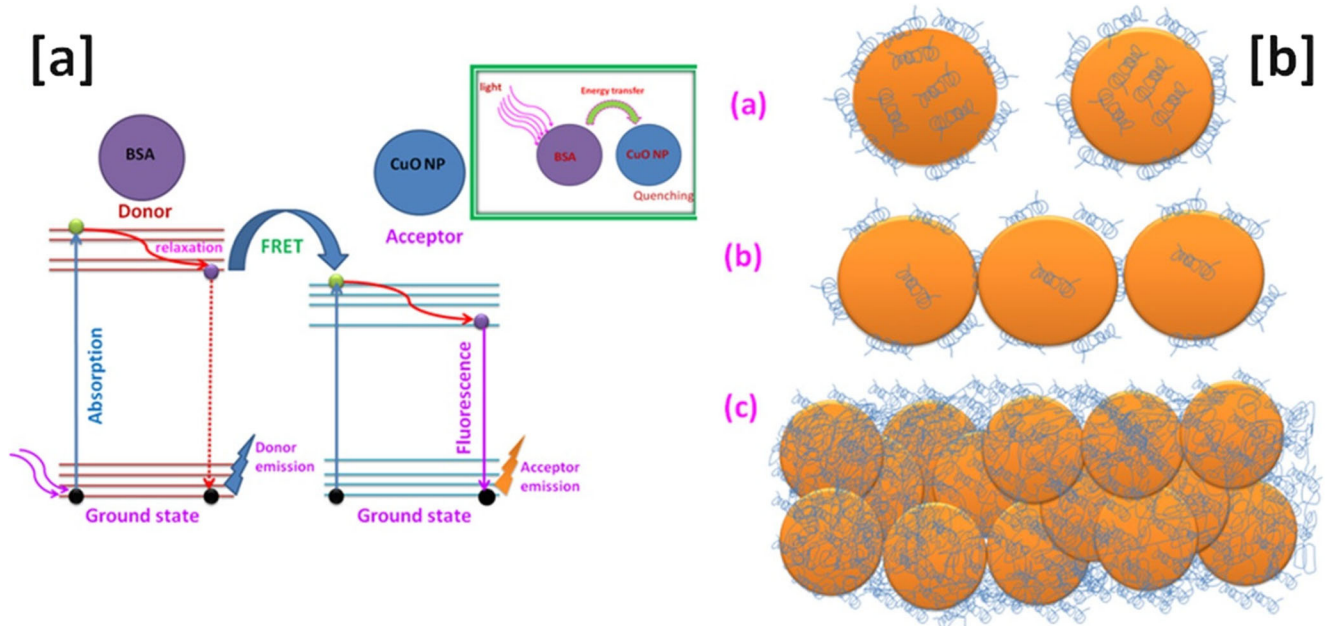


Fig. 16 **a** Schematic diagram of the energy transfer mechanism between CuO NPs–BSA bioconjugate. **b** Schematic representation of corona formation between protein and different-concentration CuO nanoparticles:

(a) small concentration of CuO NPs, (b) medium concentration of the CuO NPs, (c) large concentration of the CuO NPs

4 Conclusion

We successfully grown the CuO NPs by the cost-effective chemical precipitation method and studied their optical and structural properties. Our CuO NPs are quantum mechanically confined for a large band gap (3.60 eV) with average size 20.31 nm and 1.026eV Urbach energy. The photoluminescence spectrum of pure CuO NPs showed the formation of oxygen vacancies and multiple oxidation states of copper with strong shallow-deep-level blue emission. The crystal unit cell of the nanoparticles is found to be monoclinic with an average size of 20.31 nm and the following lattice parameters: $a = 4.568\text{\AA}$, $b = 3.4451\text{\AA}$, $c = 5.211\text{\AA}$. Our CuO nanoparticles can be utilized in semiconductor-based optoelectronic devices and in biophotonics. The observed red shifting is 3 nm and 6 nm for the absorbance of the BSA corresponding to the use of the small concentration range and large concentration range of the CuO NPs, respectively. We observe that the lower concentration of the CuO NPs leads to a large amount of protein molecules for each particle surface, whereas a large concentration of the CuO NPs leads to a small amount of protein molecules for each particle surface with the apparent association constant (K_{app}) $6.51 \times 10^3 \text{ M}^{-1}$ and $2.16 \times 10^3 \text{ M}^{-1}$, respectively. In a small concentration region, energy transfer efficiency (E_{eff}) depends on the temperature, whereas in large concentration regions, E_{eff} is almost independent of the temperature. Energy transfer strongly depends on the concentration of the CuO NPs used. The total changes in energy transfer efficiency (ΔE_{eff}) at room temperature are 22% and 5.6% for the use large and small concentrations, respectively; at body temperature, these changes are 13.6% and 6.6% for the large and small concentrations of the doses, respectively. The quenching in the fluorescence emission of tryptophan (Try) residues in the structure of BSA in the presence of CuO NPs is static in lower temperature and dynamic in higher temperature in the low-concentration range and fully dynamic in the high-concentration range. The concentration of CuO NPs affected the nature of protein denaturation process. The interaction between Try of BSA and CuO NPs is exothermic, electrostatic, and hydrophobic in nature in all concentrations of CuO NPs. Time-resolved fluorescence spectroscopy showed 79.35% energy transfer between BSA and CuO NPs which corresponds to FRET mechanism. The use of small concentration of CuO NPs represents that the core CuO NPs are fully covered by BSA with shell thickness of ~ 8 nm. The use of large concentration leads to aggregation rather than individual corona formation. This study provides important insight into the interaction of CuO nanoparticles with proteins, which may be of importance for further application of these nanoparticles in biomedical applications. The CuO NP-based energy transfer can be used effectively for biomolecular recognition and FRET-based biosensors. This report may be the important experimental report about the role of the nanoparticles concentration within the nano-bio interface science.

Acknowledgments The authors are grateful to the Department of Physics and Technophysics of Vidyasagar University and Department of Physics, Government General Degree College at Gopiballavpur-II. The authors are also thankful to CRF, IIT Kharagpur for the TEM measurement facility.

References

- Dong, X., Jiang, D., Liu, Q., Han, E., Zhang, X., Guan, X., & Qiu, B. (2014). Enhanced amperometric sensing for direct detection of nitenpyram via synergistic effect of copper nanoparticles and nitrogen-doped graphene. *Journal of Electroanalytical Chemistry*, *734*, 25–30.
- Nations, S., Long, M., Wages, M., Maul, J. D., Theodorakis, C. W., & Cobb, G. P. (2015). Subchronic and chronic developmental effects of copper oxide (CuO) nanoparticles on *Xenopus laevis*. *Chemosphere*, *135*, 166–174.
- Grigore, M. E., Biscu, E. R., Holban, A. M., Gestal, M. C., & Grumezescu, A. M. (2016). Methods of synthesis, properties and biomedical applications of CuO nanoparticles. *Pharmaceuticals*, *9*, 75. <https://doi.org/10.3390/ph9040075>.
- Perreault, F., Melegari, S. P., Da Costa, C. H., Rossetto, A. L. D. O. F., Popovic, R., & Matias, W. G. (2012). Genotoxic effects of copper oxide nanoparticles in Neuro 2A cell cultures. *Science of the Total Environment*, *441*, 117–124.
- Barua, S., Das, G., Aidew, L., Buragohain, A. K., & Karak, N. (2013). Copper–copper oxide coated nanofibrillar cellulose: a promising, biomaterial. *RSC Advances*, *3*, 14997–15004.
- Baek, Y.-W., & An, Y.-J. (2011). Microbial toxicity of metal oxide nanoparticles (CuO, NiO, ZnO, and Sb₂O₃) to *Escherichia coli*, *Bacillus subtilis*, and *Streptococcus aureus*. *Science of the Total Environment*, *409*, 1603–1608.
- Isani, G., Falcioni, M. L., Barucca, G., Sekar, D., Andreani, G., Carpenè, E., & Falcioni, G. (2013). Comparative toxicity of CuO nanoparticles and CuSO₄ in rainbow trout. *Ecotoxicology and Environmental Safety*, *97*, 40–46.
- Ostaszewska, T., Chojnacki, M., Kamaszewski, M., & Sawosz-Chwalibóg, E. (2015). Histopathological effects of silver and copper nanoparticles on the epidermis, gills, and liver of Siberian sturgeon. *Environmental Science and Pollution Research*, *23*, 1621–1633.
- Ruiz, P., Katsumiti, A., Nieto, J. A., Bori, J., Jimeno-Romero, A., Reip, P., Arostegui, I., Orbea, A., & Cajaraville, M. P. (2015). Short-term effects on antioxidant enzymes and long-term genotoxic and carcinogenic potential of CuO nanoparticles compared to bulk CuO and ionic copper in mussels *Mytilus galloprovincialis*. *Marine Environmental Research*, *111*, 107–120.
- Sankar, R., Maheswari, R., Karthik, S., Shivashangari, K. S., & Ravikumar, V. (2014). Anticancer activity of *Ficus religiosa* engineered copper oxide nanoparticles. *Materials Science and Engineering: C*, *44*, 234–239.
- Esfandfar, P., Falahati, M., & Saboury, A. (2016). Spectroscopic studies of interaction between CuO nanoparticles and bovine serum albumin. *Journal of Biomolecular Structure & Dynamics*, *34*(9), 1962–1968.
- Ingle, A. P., Duran, N., & Rai, M. (2014). Bioactivity, mechanism of action, and cytotoxicity of copper-based nanoparticles: a review. *Applied Microbiology and Biotechnology*, *98*, 1001–1009.
- Chang, Y.-N., Zhang, M., Lin, X., Zhang, J., & Xing, G. (2012). The toxic effects and mechanisms of CuO and ZnO nanoparticles. *Materials*, *5*, 2850–2871.
- Lindman, S., Lynch, I., Thulin, E., Nilsson, H., Dawson, K. A., & Linse, S. (2007). Systematic investigation of the thermodynamics of HSA adsorption to N-isopropylacrylamide/N-tert-

- butylacrylamide copolymer nanoparticles. Effects of particle size and hydrophobicity. *Nano Letters*, 7(4), 914–920.
15. Lundqvist, M., Stigler, J., Elia, G., Lynch, I., Cedervall, T., & Dawson, K. A. (2008). Nanoparticle size and surface properties determine the protein corona with possible implications for biological impacts. *Proceedings of the National Academy of Sciences of the United States of America*, 105(38), 14265–14270.
 16. Ma, Z., Bai, J., Wang, Y., & Jiang, X. (2014). Impact of shape and pore size of mesoporous silica nanoparticles on serum protein adsorption and RBCs hemolysis. *ACS Applied Materials & Interfaces*, 6(4), 2431–2438.
 17. Shang, L., & Nienhaus, G. U. (2017). In situ characterization of protein adsorption onto nanoparticles by fluorescence correlation spectroscopy. *Accounts of Chemical Research*, 50(2), 387–395.
 18. Koshkina, O., Lang, T., Thiermann, R., et al. (2015). Temperature-triggered protein adsorption on polymer-coated nanoparticles in serum. *Langmuir*, 31(32), 8873–8881.
 19. Foroozandeh, P., & Aziz, A. A. (2015). Merging worlds of nanomaterials and biological environment: factors governing protein corona formation on nanoparticles and its biological consequences. *Nanoscale Research Letters*, 10, 221.
 20. Mahmoudi, M., Abdelmonem, A. M., Behzadi, S., et al. (2013). Temperature: the 'ignored' factor at the NanoBio interface. *ACS Nano*, 7(8), 6555–6562.
 21. Klein, J. (2007). Probing the interactions of proteins and nanoparticles. *PNAS*, 104(7), 2029–2030.
 22. Zhang, T.-X., Zhu, G.-Y., Lu, B.-Y., Zhang, C.-L., & Peng, Q. (2017). Concentration-dependent protein adsorption at the nano-bio interfaces of polymeric nanoparticles and serum proteins. *Nanomedicine*, 12(22), 1–14.
 23. Bhunia, A. K., & Saha, S. (2019). Absorption spectroscopy and structural analysis of ZnO and ZnS nanostructure. *Advanced Science, Engineering and Medicine*, 11(7), 644–651.
 24. Saha, S., & Bhunia, A. K. (2013). Synthesis of Fe₂O₃ nanoparticles and study of its structural, optical properties. *Journal of Physical Sciences*, 17, 191–195.
 25. Koffyberg, F. P., & Benko, F. A. (1982). *J. Appl. Phys.*, 53, 1173.
 26. Klinbumrung, A., Thongtem, T., & Thongtem, S. (2014). Characterization and gas sensing properties of CuO synthesized by DC directly applying voltage. *Applied Surface Science*, 313, 640–646.
 27. Bhattacharjee, B., Ganguli, D., Chaudhuri, S., & Pal, A. K. (2003). Synthesis and optical characterization of sol-gel derived zinc sulphide nanoparticles confined in amorphous silica thin films. *Materials Chemistry and Physics*, 78(2), 372–379.
 28. Dhineshbabu, N. R., Rajendran, V., Nithyavathy, N., & Vetumperumal, R. (2016). Study of structural and optical properties of cupric oxide nanoparticles. *Applied Nanoscience*, 6, 933–939.
 29. Gandhi, S., Subramani, R. H. H., Ramakrishnan, T., Sivabalan, A., Dhanalakshmi, V., Nair, M. R. G., & Anbarasan, R. (2010). Ultrasound assisted one pot synthesis of nano-sized CuO and its nanocomposite with poly(vinyl alcohol). *Journal of Materials Science*, 45, 1688–1694.
 30. Suresh, Y., Annapurna, S., Bhikshamaiah, G., & Singh, A. K. (2016). Green luminescent copper nanoparticles. *IOP Conference Series: Materials Science and Engineering*, 149, 012187.
 31. Lanje, A. S., Sharma, S. J., Pode, R. B., & Raghmani, S. (2010). Ningthoujam, Synthesis and optical characterization of copper oxide nanoparticles. *Advances in Applied Science Research*, 1(2), 36–40.
 32. Zhao, X., Wang, P., Yan, Z., & Ren, N. (2015). Room temperature photoluminescence properties of CuO nanowire arrays. *Optical Materials*, 42, 544–547.
 33. Ahamed, M., Siddiqui, M. A., Akhtar, M. J., Ahmad, I., Pant, A. B., & Alhadlaq, H. A. (2010). Genotoxic potential of copper oxide nanoparticles in human lung epithelial cells. *Biochemical and Biophysical Research Communications*, 396, 578–583.
 34. Azam, A., Ahmed, A. S., Oves, M., Khan, M. S., & Memic, A. (2012). Size-dependent antimicrobial properties of CuO nanoparticles against Gram-positive and -negative bacterial strains. *International Journal of Nanomedicine*, 7, 3527–3535.
 35. Bhunia, A. K., Samanta, P. K., Kamilya, T., & Saha, S. (2015). Chemical growth of spherical zinc oxide nanoparticles and their structural, optical properties. *Journal of Physical Sciences*, 20, 205–212.
 36. Bhunia, A. K., Kamilya, T., & Saha, S. (2016). Optical and structural properties of protein capped ZnO nanoparticles and its antimicrobial activity. *Journal of Advances in Biology & Biotechnology*, 10(1), 1–9.
 37. Kahouli, M., Barhoumi, A., Al-Hajry, A., & Guermazi, S. (2015). Structural and optical properties of ZnO nanoparticles prepared by direct precipitation method. *Superlattices and Microstructures*, 85, 7–23.
 38. Dar, M. A., Ahsanulhaq, Q., Kim, Y. S., Sohn, J. M., Kim, W. B., & Shin, H. S. (2009). Versatile synthesis of rectangular shaped nanobatch-like CuO nanostructures by hydrothermal method; structural properties and growth mechanism. *Applied Surface Science*, 255, 6279–6284.
 39. Bhunia, A. K., Samanta, P. K., Saha, S., & Kamilya, T. (2013). ZnO nanoparticle-protein interaction: corona formation with associated unfolding. *Applied Physics Letters*, 103, 143701.
 40. Bhunia, A. K., Kamilya, T., & Saha, S. (2016). Temperature dependent and kinetic study of the adsorption of bovine serum albumin to ZnO nanoparticle surfaces. *ChemistrySelect*, 1, 2872–2882.
 41. Zhang, T.-X., Zhu, G.-Y., Lu, B.-Y., Zhang, C.-L., & Peng, Q. (2017). Concentration-dependent protein adsorption at the nano-bio interfaces of polymeric nanoparticles and serum proteins. *Nanomedicine (London, England)*, 12(22), 2757–2769.
 42. Kathiravan, A., Paramaguru, G., & Renganathan, R. (2009). Study on the binding of colloidal zinc oxide nanoparticles with bovine serum albumin. *Journal of Molecular Structure*, 934, 129–137.
 43. Benesi, H. A., & Hildebrand, J. H. (1949). *Journal of the American Chemical Society*, 71, 2703–2707.
 44. Lakowicz, J. R. (2006). *Principles of Fluorescence Spectroscopy* (3rd ed.) XXVI, 954. Springer.
 45. Bhunia, A. K., Kamilya, T., & Saha, S. (2016). Photo relaxation change and emission quenching in different sizes of PbS-nanoparticles-protein corona. *ChemistrySelect*, 1, 5768–5778.
 46. Majorek, K. A., Porebski, P. J., Dayal, A., Zimmerman, M. D., Jablonska, K., Stewart, A. J., Chruszcz, M., & Minor, W. (2012). Structural and immunologic characterization of bovine, horse, and rabbit serum albumins. *Molecular Immunology*, 52(3–4), 174–182.
 47. Cowgill, R. W. (1967). *Acta Protein Structure*, 140, 37–44.
 48. Geldert, K. A., Liu, Y., Loh, K. P., & Lim, C. T. (2017). Nano-bio interactions between carbon nanomaterials and blood plasma proteins: why oxygen functionality matters. *NPG Asia Materials*, 9(1–12), e422.
 49. Ansari, A., Sachar, S., & Garje, S. S. (2018). Synthesis of bare and surface modified TiO₂ nanoparticles via a single source precursor and insights into their interactions with serum albumin. *New Journal of Chemistry*, 42, 13358–13366.
 50. Wang, G., Hou, H., Wang, S., Yan, C., & Liu, Y. (2017). Exploring the interaction of silver nanoparticles with lysozyme: Binding behaviors and kinetics. *Colloids and Surfaces B: Biointerfaces*, 157, 138–145.
 51. Bhunia, A. K., Kamilya, T., & Saha, S. (2017). Silver nanoparticle-human hemoglobin interface: time evolution of the corona formation and interaction phenomenon. *Nano Convergence*, 4, 28,1–28, 2812.
 52. Bhunia, A. K., Samanta, P. K., Saha, S., & Kamilya, T. (2014). Safety concerns towards the biomedical application of PbS

- nanoparticles: an approach through protein-PbS interaction and corona formation. *Applied Physics Letters*, 104, 123703.
53. Esfandfara, P., Falahati, M., & Saboury, A. A. (2016). Spectroscopic studies of interaction between CuO nanoparticles and bovine serum albumin. *Journal of Biomolecular Structure and Dynamics*, 34(9)1962–1968.
 54. Bhogalea, A., Patel, N., Sarpotdar, P., Mariam, J., Dongre, P. M., Miotello, A., & Kothari, D. C. (2013). *Colloids and Surfaces, B: Biointerfaces*, 102, 257–264.
 55. Hao, C., Xu, G., Feng, Y., Lu, L., Sun, W., & Sun, R. (2017). Fluorescence quenching study on the interaction of ferroferric oxide nanoparticles with bovine serum albumin. *Spectrochimica Acta Part A: Molecular and Biomolecular Spectroscopy*, 184, 191–197.
 56. Wang, G., Lu, Y., Hou, H., & Liu, Y. (2017). Probing the binding behavior and kinetics of silver nanoparticles with bovine serum albumin. *RSC Advances*, 7, 9393–9401.
 57. Hill, A. V. (1913). *The Biochemical Journal*, 7, 471–480.
 58. Hill, A. V. (1921). *The Biochemical Journal*, 15, 577–586.
 59. Abraham, A. N., Sharma, T. K., Bansal, V., & Shukla, R. (2018). Phytochemicals as dynamic surface ligands to control nanoparticle–protein interactions. *ACS Omega*, 3, 2220–2229.
 60. Markarian, S. A., & Aznauryan, M. G. (2012). Study on the interaction between isoniazid and bovine serum albumin by fluorescence spectroscopy: the effect of dimethylsulfoxide. *Molecular Biology Reports*, 39, 7559–7567.
 61. Mudunkotuwa, I. A., & Grassian, V. H. (2014). Histidine adsorption on TiO₂ nanoparticles: an integrated spectroscopic, thermodynamic, and molecular-based approach toward understanding nanobio interactions. *Langmuir*, 30(29), 8751–8760.
 62. Ahmad, F., Zhou, Y., Ling, Z., Xiang, Q., & Zhou, X. (2016). Systematic elucidation of interactive unfolding and corona formation of bovine serum albumin with cobalt ferrite nanoparticles. *RSC Advances*, 6, 35719–35730.
 63. Arai, T., & Norde, W. (1990). *Colloids and Surfaces*, 51, 17–28.
 64. Lynch, I., & Dawson, K. A. (2008). *Nano Today*, 3, 40–47.
 65. Sun, B., Zhang, Y., Chen, W., Wang, K., & Zhu, L. (2018). Concentration dependent effects of bovine serum albumin on graphene oxide colloidal stability in aquatic environment. *Environmental Science & Technology*, 52(13), 7212–7219.
 66. Röcker, C., Pötz, M., Zhang, F., Parak, W. J., & Nienhaus, G. U. (2009). A quantitative fluorescence study of protein monolayer formation on colloidal nanoparticles. *Nature Nanotechnology*, 4, 577–580.
 67. Rainbow, M. R., Atherton, S., & Eberhart, R. C. (1987). *Journal of Biomedical Materials Research*, 21(5), 539–555.
 68. Gao, D., Tian, Y., Bi, S., Chen, Y., Yu, A., & Zhang, H. (2005). *Spectrochimica Acta, Part A: Molecular and Biomolecular Spectroscopy*, 62, 1203–1208.
 69. Patel, A. S., Mishra, P., Kanaujia, P. K., Husain, S. S., Prakash, G. V., & Chakraborti, A. (2017). Investigating resonance energy transfer from protein molecules to van der Waals nanosheets. *RSC Advances*, 7, 26250.
 70. Elangovan, M., Day, R. N., & Periasamy, A. (2002). Nanosecond fluorescence resonance energy transfer-fluorescence lifetime imaging microscopy to localize the protein interactions in a single living cell. *Journal of Microscopy*, 205(1), 3–14.
 71. Protein Data Bank (PDB).

Publisher's Note Springer Nature remains neutral with regard to jurisdictional claims in published maps and institutional affiliations.